

# Structural and electrochemical properties of spray deposited molybdenum trioxide ( $\alpha$ -MoO<sub>3</sub>) thin films

S. A. Khalate<sup>1</sup> · R. S. Kate<sup>1</sup> · H. M. Pathan<sup>2</sup> · R. J. Deokate<sup>1</sup>

Received: 20 December 2016 / Revised: 2 February 2017 / Accepted: 10 February 2017 / Published online: 25 February 2017  
© Springer-Verlag Berlin Heidelberg 2017

**Abstract** Nanostructured molybdenum trioxide ( $\alpha$ -MoO<sub>3</sub>) thin films were deposited to investigate effect of substrate temperature on microstructural, morphological, optical, electrical, and electrochemical properties of the  $\alpha$ -MoO<sub>3</sub> thin films. X-ray diffraction results indicated deposited  $\alpha$ -MoO<sub>3</sub> thin films are polycrystalline, crystallizes in orthorhombic structure, and crystalline quality improved with substrate temperature. Films show the optical band gap varied between 2.56 and 2.85 eV, the activation energy of the  $\alpha$ -MoO<sub>3</sub> thin films were found to be in the range of 0.15–0.30 eV. The measured electrochemical properties of  $\alpha$ -MoO<sub>3</sub> thin film electrode deposited at 673 K exhibits significantly improved supercapacitive performance in Na<sub>2</sub>SO<sub>4</sub> (0.5 M) electrolyte about 73.61 F/g at current density 0.6 mA/cm<sup>2</sup> than the other deposition temperatures. The maximum energy density (11.13 Wh/kg) at the power density 10.54 kW/kg was observed.

**Keywords** Orthorhombic phase · Nanorods · Optical properties · Electrochemical

## Introduction

Recently, use of nanomaterial supercapacitor electrodes has been attracting great interest due to their high power and energy densities than the respective bulk materials [1]. According to the energy storage mechanism, supercapacitors are classified into

two categories, namely, electrical double-layer capacitors (EDLC) with carbon materials as electrodes and pseudocapacitors with metal oxide or conducting polymers. Previous research has shown several important factors affecting the performance of EDLC: specific area, electrical conductivity, pore size, and distribution [2]. However, the low-energy density, especially the low volumetric energy density of EDLC materials is yet to be improved. The pseudocapacitors store energy through a Faradic process that involves fast and reversible redox reactions occurring at or near the electrode surface [3–5]. The most widely explored pseudocapacitive electrode materials include transition metal oxides or hydroxides (MnO<sub>2</sub>, V<sub>2</sub>O<sub>5</sub>, RuO<sub>2</sub>, Co<sub>3</sub>O<sub>4</sub>, NiO, MoO<sub>3</sub>, etc.) [6–11]; among these electrode materials for pseudocapacitors, MoO<sub>3</sub> has been extensively investigated due to its natural abundance, large theoretical capability, and low toxicity [12]. Moreover, MoO<sub>3</sub> have attracted much attention as pseudocapacitive electrode material due to its crystallographic structure, multiple oxidation states, n-type conductivity, etc. [13–15].

Different techniques like hydrothermal method [16], sputtering [17], atomic layer deposition [18], sol-gel [19], chemical vapor deposition [20, 21], molecular beam epitaxy [22], and spray pyrolysis [23–26] have been used to prepare the  $\alpha$ -MoO<sub>3</sub> thin films. Among them, spray pyrolysis coating is a simple and low-cost method for the preparation of thin films with large areas. This method is convenient for preparing pinhole free, homogenous and smoother films with the required substrate temperature. It is very attractive because it has been largely used to produce oxides [27] and sulfides [28] of II–VI group semiconductors.

In this investigation,  $\alpha$ -MoO<sub>3</sub> thin films with nanostructured rod are deposited on FTO substrates by spray pyrolysis method. The effect of substrate temperature on structural, morphological, and supercapacitive properties of  $\alpha$ -MoO<sub>3</sub> thin films has been calculated. Further electrochemical characteristics like cyclic

✉ R. J. Deokate  
rjdeokate@gmail.com

<sup>1</sup> Vidya Pratishthan's Arts Science and Commerce College,  
Baramati, MS, India

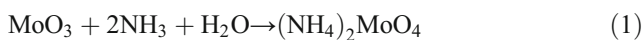
<sup>2</sup> Department of Physics, Savitribai Phule Pune University, Pune, India

voltammetry, galvanostatic charge/discharge measurement, specific capacitance, energy density, and power density were studied and reported.

## Experimental details

### Deposition of $\alpha$ -MoO<sub>3</sub> thin films

Molybdenum trioxide ( $\alpha$ -MoO<sub>3</sub>) thin films were deposited onto glass substrates via well-known spray pyrolysis technique. The spraying solution consisted of 0.1 M molybdenum trioxide powder (AR grade, SD fine, 99.5% pure) dissolved in ammonia solution separately to form ammonium molybdate at room temperature. The undergoing chemical reaction is given in the following equation:



The solution was sprayed onto the glass substrates at various substrate temperatures within 573–723 K. The pyrolytic decomposition of (NH<sub>4</sub>)<sub>2</sub>MoO<sub>4</sub> on the surface of the substrates results in the formation of  $\alpha$ -MoO<sub>3</sub> thin films according to the following equation:



The temperature of the substrate controlled within  $\pm 1$  K through temperature controller. During the deposition, other parameters, especially spray rate (5 cm<sup>3</sup>/min), nozzle to substrate distance (NSD) (32 cm), etc., were kept at their fixed values [28]. The sprayed droplets undergo evaporation and solute condensation, and thermal decomposition resulted in well adherent molybdenum trioxide thin films.

### Characterization

For thickness measurement, gravimetric weight difference method is used with the relation of  $t = m/(\rho \times A)$ , where  $m$  is the mass of the film deposited on the substrate in grams,  $A$  is the area of the deposited film in square centimeters, and  $\rho$  is the density of the deposited material (MoO<sub>3</sub> = 4.69 g/cm<sup>3</sup>) in bulk form. The structural properties of  $\alpha$ -MoO<sub>3</sub> thin films were carried out by x-ray diffractometer (XRD Bruker AXS D8 Advance Model) with the radiation source Cu-K $\alpha$  ( $\lambda = 1.5406 \text{ \AA}$ ) at  $2\theta$  in the range 20 to 80°. Surface morphology of the deposited  $\alpha$ -MoO<sub>3</sub> thin films was studied with field emission scanning electron microscope (FE-SEM SU8000 Hitachi). The optical parameters were studied at room temperature in the wavelength range 400–900 nm through UV-Visible spectroscopy (PerkinElmer Lambda 1050 UV-Vis-NIR Spectrophotometer). Surface electrical study was carried out by standard two-probe resistivity method. The electrochemical measurements of the  $\alpha$ -MoO<sub>3</sub> thin film electrodes were reported using cyclic voltammetry (CV) and galvanostatic

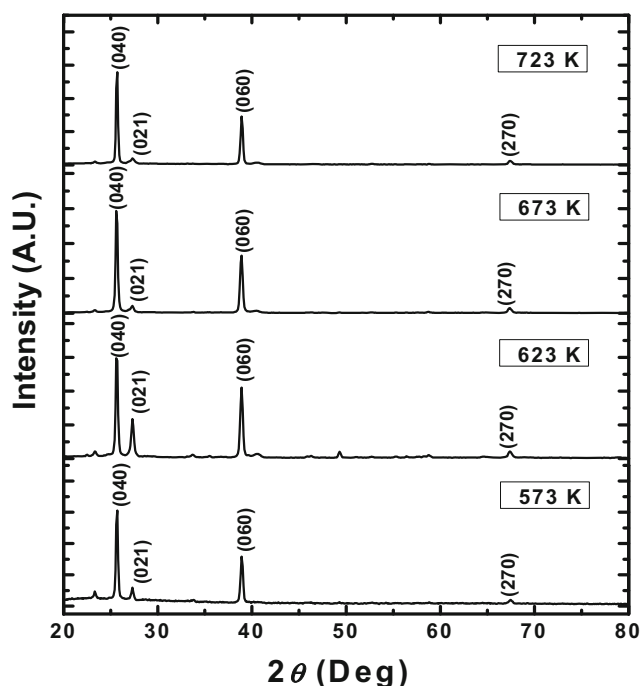


**Fig. 1** X-ray diffraction patterns of  $\alpha$ -MoO<sub>3</sub> thin films deposited for different substrate temperatures

analysis. A potentiostat (CHI 6005E, made in USA) and a (CHI 6002E, made in USA) were used with three-electrode electrochemical cell containing Na<sub>2</sub>SO<sub>4</sub> (0.5 M) as the electrolyte,  $\alpha$ -MoO<sub>3</sub> as the working electrode, Ag/AgCl as the reference electrode, and platinum wire as the counter electrode.

## Results and discussion

### X-ray diffraction studies

Figure 1 shows the typical XRD pattern of  $\alpha$ -MoO<sub>3</sub> thin films deposited at various substrate temperatures (573–723 K). The observed diffraction peaks at  $2\theta^\circ$  are around 25.7, 27.3, 38.9,

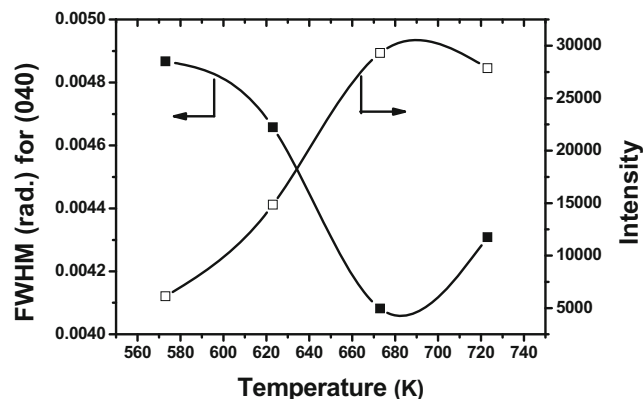


**Fig. 2** Plot of FWHM and relative peak intensity of (0 4 0) diffraction peak for  $\alpha$ -MoO<sub>3</sub> thin films at different substrate temperatures

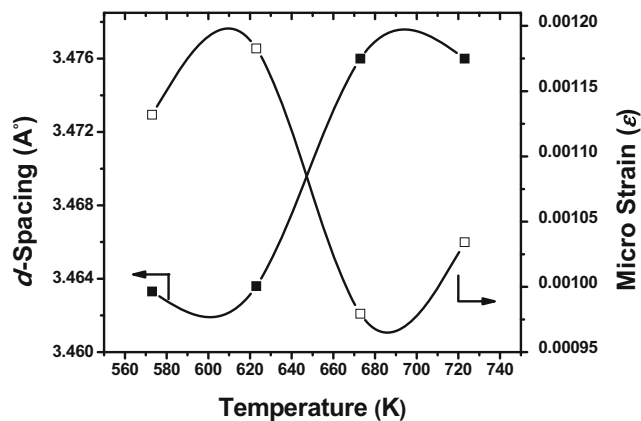


**Fig. 3** The variation of microstrain and interplanar spacing of  $\alpha$ -MoO<sub>3</sub> thin film for different substrate temperatures

and 67.4 with the corresponding Miller ( $h k l$ ) planes (0 4 0), (0 2 1), (0 6 0), and (2 7 0), respectively. All these observed peaks correspond to stable orthorhombic  $\alpha$ -MoO<sub>3</sub> phase according to the standard JCPDS data card: 01-0706 [29], Liqiang Mai, et al. reported the similar results [30]. Figure 1 depicts integrated intensities of the diffraction peaks suggests that  $\alpha$ -MoO<sub>3</sub> thin films grow in the preferential orientation (0  $k$  0) direction where,  $k = 4, 6$ . The (0 4 0) peaks are dominating preferential growth with  $b$ -axis perpendicular to the surface of all thin films. However, other phases and structural rearrangements are not observed in the  $\alpha$ -MoO<sub>3</sub> thin films prepared at temperature range of 573–723 K. The lattice parameters  $a, b$ , and  $c$  for orthorhombic phase was determined by using the following equation:

$$d_{(hkl)} = \frac{1}{\sqrt{\frac{h^2}{a^2} + \frac{k^2}{b^2} + \frac{l^2}{c^2}}} \tag{3}$$

For orthorhombic lattice,  $a \neq b \neq c$ , in the above relation,  $h, k$ , and  $l$  are Miller indices of reflector planes appearing on the diffraction spectrum and  $d_{(hkl)}$  is their interplanar distance. The obtained average lattice constants were found to be  $a = 3.95 \text{ \AA}$ ,  $b = 13.84 \text{ \AA}$ , and  $c = 3.69 \text{ \AA}$ . These values are consistent with standard JCPDS data card [29]. The interplanar distances were calculated by the following equation:

$$2d\sin\theta = n\lambda \tag{4}$$

where  $d$  is the interplanar distance,  $\theta$  is the Bragg's angle,  $n$  is the order of diffraction (usually  $n = 1$ ), and  $\lambda$  is the wavelength of the x-ray used (here,  $\lambda = 1.5406 \text{ \AA}$ ). The average crystallite size ( $D$ ) of the prepared films was calculated by the Scherrer relation [31]:

$$D = \frac{k\lambda}{\beta\cos\theta} \tag{5}$$

where  $k$  is the shape factor with value  $k = 0.94$ ,  $\lambda$  is the wavelength of the x-ray used ( $\lambda = 1.5406 \text{ \AA}$ ),  $\beta$  is the full width at half maxima (FWHM) of corresponding peak, and  $\theta$  is the Bragg's angle. The average crystallite size of the  $\alpha$ -MoO<sub>3</sub> film initially increase with substrate

**Table 1** The microstructural properties of  $\alpha$ -MoO<sub>3</sub> thin films deposited for different substrate temperature

Temp. [°C]	$h$	$k$	$l$	$2\theta_{(obs.)}$	$d_{(obs.)} (\text{\AA})$	FWHM	Intensity	Crystallite size (nm)	Dislocation density	Microstrain ( $\epsilon$ ) $\times 10^{-3}$
300	0	4	0	25.607	3.4633	0.004867	6125	29.21496	1.17E + 15	1.131830388
	0	4	0	27.305	3.2636	0.005024	1188	28.40075	1.24E + 15	0.66692865
	0	6	0	38.899	2.3132	0.005251	3175	28.00478	1.28E + 15	1.101452514
	2	7	0	67.399	1.3878	0.007955	406	20.95141	2.28E + 15	1.65455839
350	0	4	0	25.607	3.4636	0.004658	14,857	30.52804	1.07E + 15	1.182700863
	0	4	0	27.305	3.2639	0.005726	5877	24.93728	1.61E + 15	0.585187588
	0	6	0	38.903	2.313	0.005338	10,519	27.54681	1.32E + 15	1.081968871
	2	7	0	67.401	1.3865	0.008077	1077	20.63459	2.35E + 15	1.67988425
400	0	4	0	25.7	3.476	0.004082	29,313	34.83979	8.24E + 14	0.979440986
	0	4	0	27.3	3.2635	0.007187	2134	19.85295	2.54E + 15	0.837143226
	0	6	0	38.906	2.3134	0.00478	16,524	30.76438	1.06E + 15	0.984915041
	2	7	0	67.503	1.3883	0.006873	1490	24.25199	1.70E + 15	1.42864767
450	0	4	0	25.702	3.476	0.004309	27,870	33.00605	9.18E + 14	1.034154469
	0	4	0	27.305	3.2636	0.003716	1983	38.40067	6.78E + 14	0.434847686
	0	6	0	38.903	2.3132	0.005007	14,566	29.37113	1.16E + 15	1.030580858
	2	7	0	67.427	1.3883	0.007885	1205	21.14939	2.24E + 15	1.63973181

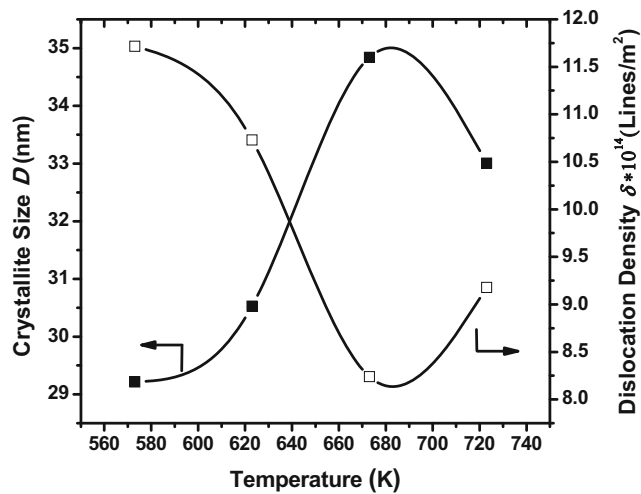


**Fig. 4** Crystallite size and dislocation density of  $\alpha$ -MoO<sub>3</sub> thin film for different substrate temperatures

temperature reaches maximum 34.83 nm at 673 K further decreased with high substrate temperature. Increases in crystallinity and crystallite size with substrate temperature are due to the optimum rate of supply of thermal energy for the recrystallization [32]. The graphical representation of intensity and the FWHM of the peak (0 4 0) with respect to substrate temperature is given in Fig. 2. The sum of individual intensities scattered by each grain is the total intensity of all grains [26]. The FWHM values are seen to decrease with substrate temperature up to 673 K and further found to increase at high temperature. However, the stresses are one of the most important unfavorable factors affecting the structural properties and geometric mismatch at boundaries between crystalline lattices of films and substrates [33]. The microstrains are

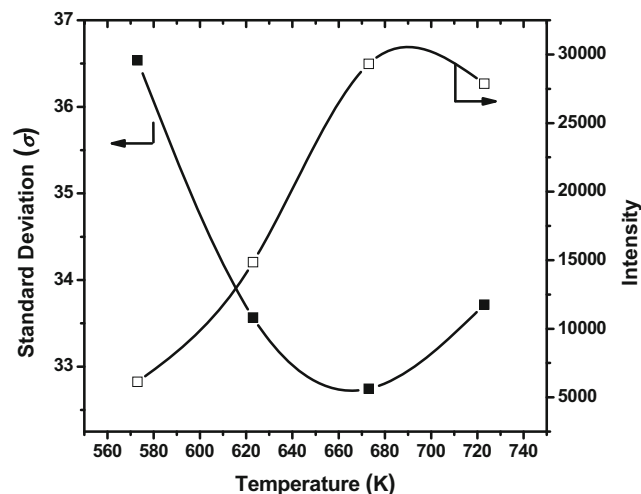


**Fig. 5** The variation of standard deviation and intensity of  $\alpha$ -MoO<sub>3</sub> thin film for different substrate temperatures

developed in the films due to these stresses. The microstrains are calculated by the following relation [34]:

$$\varepsilon = \frac{\beta \cos \theta}{4} \quad (6)$$

The existence of internal microstrain can easily induce the formation of defect centers [35]. The dislocation density ( $\delta$ ) values can be obtained by following relations [36]:

$$\delta = \frac{1}{D^2} \quad (7)$$

The variation in microstructural parameters like microstrain and interplanar spacing with substrate temperature is shown in Fig. 3. The interplanar spacing of  $\alpha$ -MoO<sub>3</sub> thin films are increases with substrate temperature consequently microstrain relaxation in  $\alpha$ -MoO<sub>3</sub> thin films decreases. The microstrain relaxation is steady with the contraction or expansion of the interplanar spacing of (0 4 0) plane. Table 1 gives the values of microstructural properties of the  $\alpha$ -MoO<sub>3</sub> films. The graphical nature of crystallite size ( $D$ ) and dislocation density ( $\delta$ ) with different substrate temperature of  $\alpha$ -MoO<sub>3</sub> thin films is shown in Fig. 4. The dislocation density of the films decreased up to 673 K further increased with substrate temperature. In order to explain growth mechanism involved in sprayed  $\alpha$ -MoO<sub>3</sub> films, the standard deviation ( $\sigma$ ) in intensities of various planes was calculated by using the following equation (Fig. 5) [37]:

$$\sigma = \sqrt{\frac{\sum_N (I)^2 - \frac{(\sum I)^2}{N}}{N}} \quad (8)$$

where  $I$  stand for the relative intensity of the ( $hkl$ ) plane and  $N$  is the reflection number. The standard deviation ( $\sigma$ ) value was found between 36.53 and 32.74, the decrease in standard deviation at high temperature is due to improved crystallinity and reorientational effects. The reflection intensities from each XRD pattern contain information related to the preferential or random growth of polycrystalline thin films which is studied by calculating the texture coefficient  $TC_{(hkl)}$  for all planes using the following equation [38]:

$$TC_{(hkl)} = \frac{\frac{I_{hkl}}{I_{0hkl}}}{\frac{1}{N} \sum_N \frac{I_{hkl}}{I_{0hkl}}} \quad (9)$$

where  $I_{hkl}$  is the relative intensity of the observed peak,  $I_{0hkl}$  is the corresponding standard relative intensity from the JCPDS

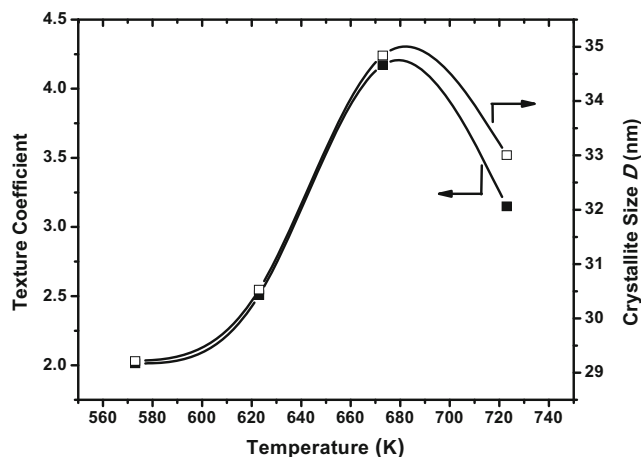


**Fig. 6** Texture coefficient and crystallite size of  $\alpha$ -MoO<sub>3</sub> thin film for different substrate temperatures

data and  $N$  is the number of reflections observed in the pattern. From Eq. (9), it is observed that the value of TC is greater than unity when the  $(h k l)$  plane is preferentially oriented. Figure 6

shows the variation of the TC for  $(0 4 0)$  plane with respect to substrate temperature for  $\alpha$ -MoO<sub>3</sub> thin films. Figure 6 shows that the lower value of texture coefficient represents that the films have poor crystallinity and the crystallinity improved with substrate temperature. Further, with increase in substrate temperature above 673 K, the value of texture coefficient slightly decreases.

**Field-emission scanning electron microscopy**

The surface morphology was determined using field-emission scanning electron microscopy (FE-SEM) and compared with XRD data. Figure 7 shows surface morphology of  $\alpha$ -MoO<sub>3</sub> thin films prepared at different substrate temperatures. At low substrate temperature (573 K),  $\alpha$ -MoO<sub>3</sub> thin film shows surface morphology with dense surface and reticulated oblate-structured grains. However, at high substrate temperature, grain boundaries increased and few small nanorods were observed. At 673 K substrate temperature, typical one-

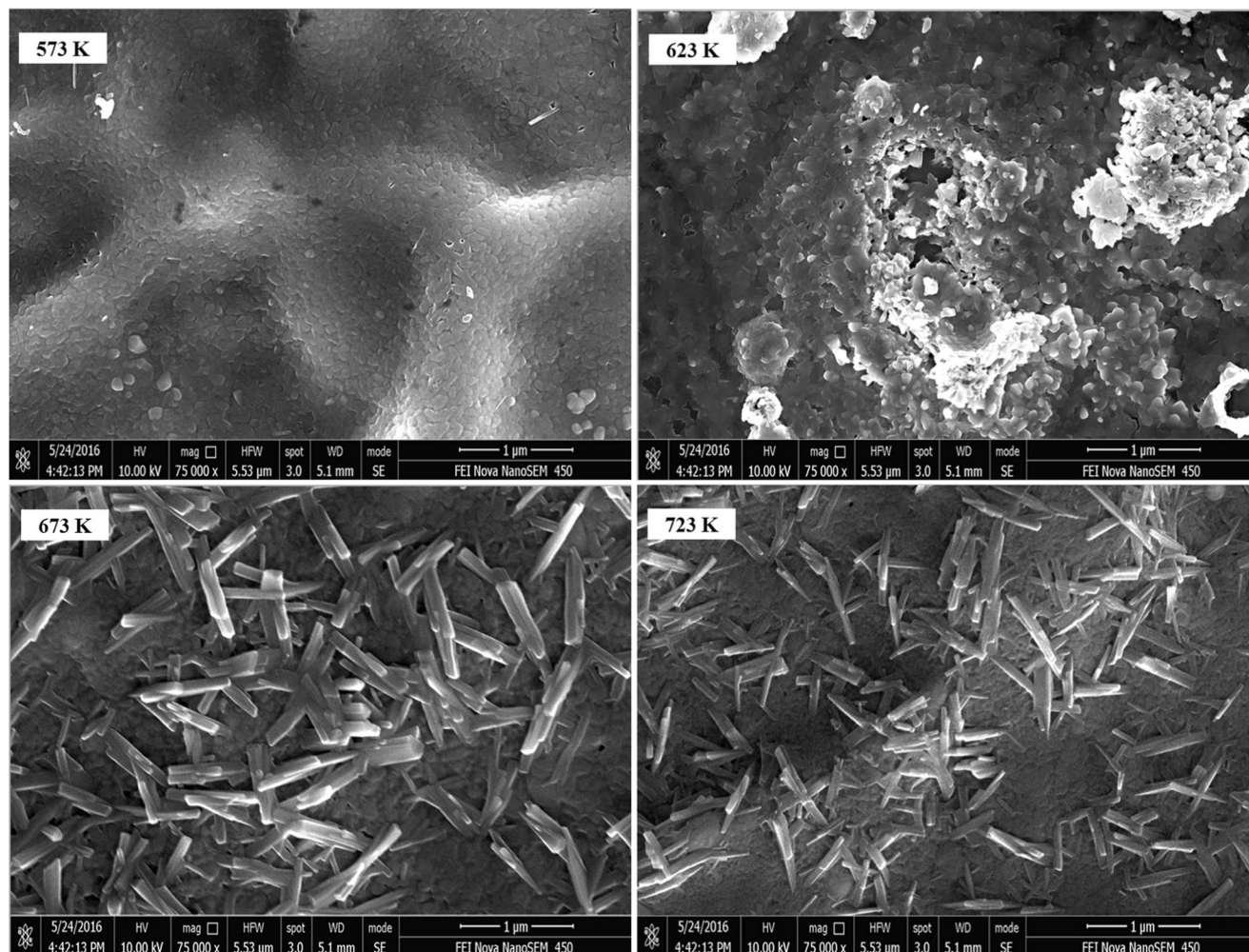


**Fig. 7** Surface FE-SEM images of  $\alpha$ -MoO<sub>3</sub> thin film for different substrate temperature

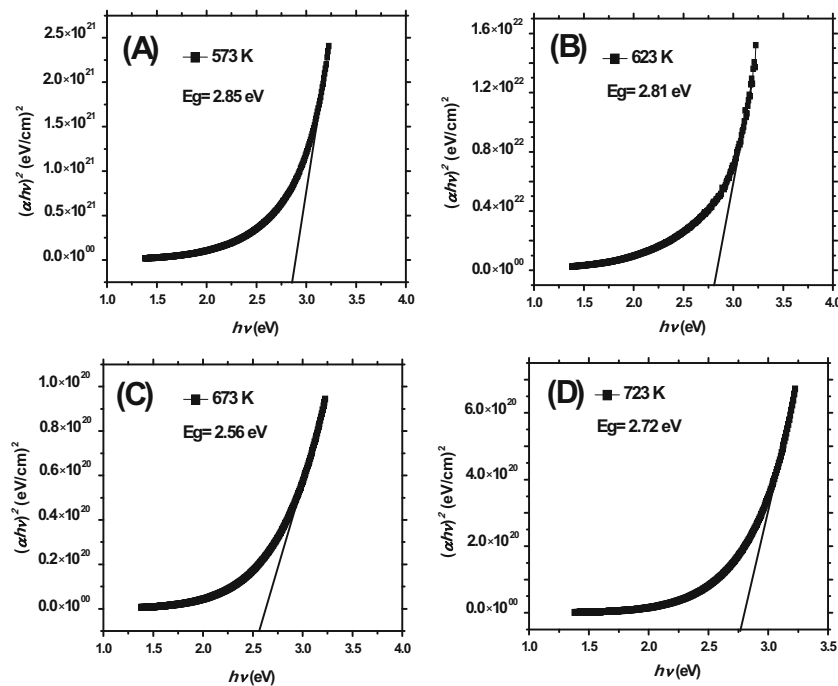


**Fig. 8** a Plot of  $(\alpha h\nu)^2$  vs. the photon energy ( $h\nu$ ) of  $\alpha$ -MoO<sub>3</sub> thin films for different substrate temperature. b The variation of optical band gap of  $\alpha$ -MoO<sub>3</sub> thin film for different substrate temperatures

dimensional nanorod-like morphology formed and such rods grow larger due to enhanced surface diffusion of species.

### Optical properties

The optical band gap energy  $E_g$  can be determined from the experimental values of absorption coefficient as a function of photon energy  $h\nu$ , using the following equation: [39]:

$$(\alpha h\nu)^n = A(h\nu - E_g) \quad (10)$$

where  $A$  is the probability parameter for the transition,  $\alpha$  is the optical absorption coefficient,  $E_g$  is the band gap energy,  $h\nu$  is

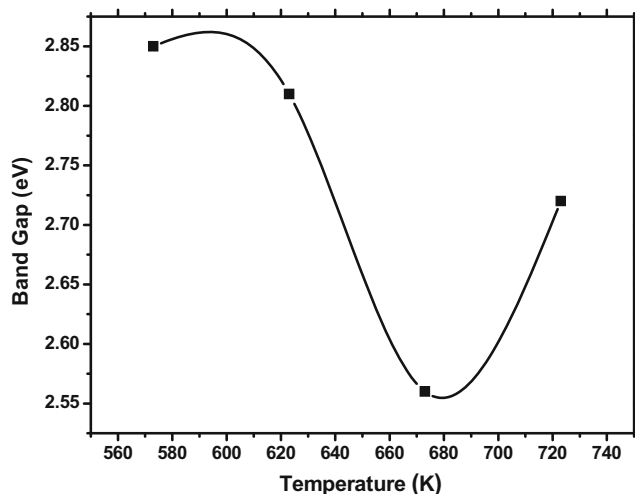


**Fig. 8** continued.

the photon energy, and exponent  $n$  determines the type of electronic transitions causing the absorption and take the values (1/2 for indirect transitions and 2 for the direct transitions). The plot of  $(\alpha h\nu)^2$  vs. ( $h\nu$ ) is shown in Fig. 8a which is linear at absorption edge, indicating a direct allowed transition. The band gap energy is found to be in the range 2.56 to 2.85 eV depending upon substrate temperature and the variation is depicted in Fig. 8b [40]. The change in band gap energy is due to the effect of internal compressive stress and various chemical compositions [35]. At higher temperature, internal compressive stress releases the crystal, and expansion of lattice will reduce the band gap of  $\alpha$ -MoO<sub>3</sub> films [41, 42]. The internal compressive stress relaxation has been confirmed by the XRD. With increasing substrate temperature, the grain size increases and the grain boundary density decreases; the scattering of electron at grain boundaries decreases resulted in electronic transition from valance band to conduction band becoming easy.

### Electrical properties

The measurement of surface electrical resistance of the  $\alpha$ -MoO<sub>3</sub> thin films was using standard two-probe method in the temperature range 573–723 K. A plot of inverse absolute temperature ( $1000/T$ ) vs.  $\log(\rho)$  for a cooling cycle is shown in Fig. 9a. Decrease in electrical resistance behavior with increasing substrate temperature may be due to the increase in the crystallite size. This is attributed to the crystallite boundary discontinuities, presence of surface states, and the change in

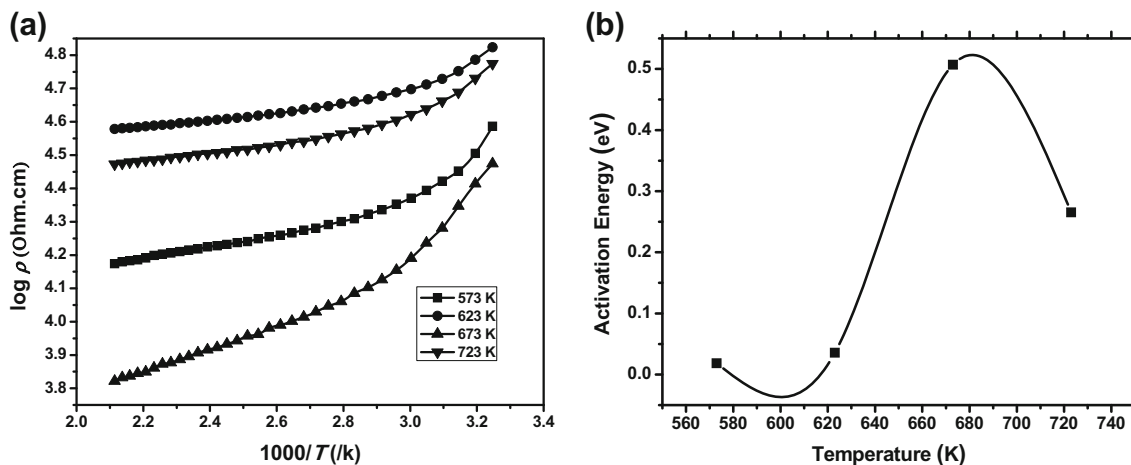


**Fig. 9** **a** Plot of surface electrical resistance versus temperature of  $\alpha$ -MoO<sub>3</sub> thin films at different substrate temperatures. **b** Plot of activation energy of the  $\alpha$ -MoO<sub>3</sub> thin films at different substrate temperatures

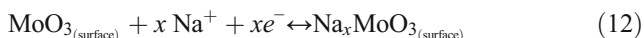
structural parameter of the thin films. Activation energy of the  $\alpha$ -MoO<sub>3</sub> thin films is calculated by the following equation:

$$\rho(T) = \rho_0 \exp\left(\frac{E_a}{K_B T}\right) \tag{11}$$

where  $\rho(T)$  is the resistivity at absolute temperature  $T$ ,  $E_a$  is the thermal activation energy, and  $K_B$  is the Boltzmann constant. The  $E_a$  is found to be in the range between 0.15 and 0.50 eV, indicating that the prepared samples are semiconductors. This change in energy attributed to change in dislocation and the stoichiometry of the films. The graphical representation of the activation energy is shown in Fig. 9.

### Electrochemical properties

To study electrochemical properties of prepared  $\alpha$ -MoO<sub>3</sub> thin film electrodes, the cyclic voltammetry (CV) is carried in Na<sub>2</sub>SO<sub>4</sub> electrolyte. The representation of electrochemical Na<sup>+</sup> insertion process is given by the following equation:



where  $x = QM/mF$  is the mole fraction of Na<sup>+</sup> insertion. Here,  $Q$  is the stored charge,  $M$  is the molar weight,  $m$  is the mass, and  $F$  is the Faraday constant. During intercalation/de-intercalation process, two mechanisms occur: the first mechanism is based on simple surface adsorption of alkali metal cations such as Na<sup>+</sup> in the electrolyte on the surface of electrode material, and the second mechanism involves the intercalation of alkali metal cations (Na<sup>+</sup>) into the electrode material during reduction and de-intercalation upon oxidation [43].

Figure 10a shows the cyclic voltammograms (CVs) of  $\alpha$ -MoO<sub>3</sub> thin film deposited at substrate temperature 673 K in a potential range of  $-0.5$  to  $+0.2$  V vs. Ag/AgCl at different scan rates. The area under the curve increased continuously with a

scan rate from 5 to 100 mV/s. At low scan rate 5 mV/s, the oxidation and reduction peaks are observed approximately at  $-0.32$  and  $-0.21$  V vs. Ag/AgCl, respectively. This is different from the reported ordered mesoporous  $\alpha$ -MoO<sub>3</sub> [44]; this may be due to the different morphology and structure. As usual, the intensities of the redox peaks increased with the scan rate. The redox peaks are shifted slightly due to the increase in over potentials. The oxidation and reduction peaks are observed at  $-0.35$  and  $-0.17$  V vs. Ag/AgCl reference electrode, respectively, at a scan rate of 100 mV/s. The redox peaks are still evident even at high scan rate of 100 mV/s, represents that  $\alpha$ -MoO<sub>3</sub> thin film electrodes will be stable as an anode material for supercapacitors and present good rate capability [45]. The specific capacitance ( $C_s$ ) was calculated using following relations [46]:

$$C = \frac{I}{dv/dt}, C_i = \frac{C}{A} \text{ and } C_s = \frac{C_i}{m} \tag{13}$$

where  $C$  is the differential capacitance,  $I$  is the average current in ampere,  $dv/dt$  is the voltage scanning rate,  $C_i$  is the interfacial capacitance,  $A$  is the area of active material dipped in the electrolyte, and  $m$  is the weight of  $\alpha$ -MoO<sub>3</sub> film dipped in electrolyte. The specific capacitance value found to be 118.79 F/g at the scan rate of 100 mV/s for the  $\alpha$ -MoO<sub>3</sub> thin film electrode deposited at substrate temperature 673 K.

The galvanostatic charge/discharge curves at different current densities (0.6 to 0.9 mA/cm<sup>2</sup>) of the electrode prepared at 673 K are shown in Fig. 10b. The figure shows that charge/discharge time decreases with the increase in applied current density. The galvanostatic charge/discharge (GCD) curves are almost linear and symmetrical without IR drop, indicating a rapid I–V response and good capacitance performance [47]. The inset of Fig. 10c shows galvanostatic charge/discharge curves of the last few cycles at 0.6 mA/cm<sup>2</sup> current density

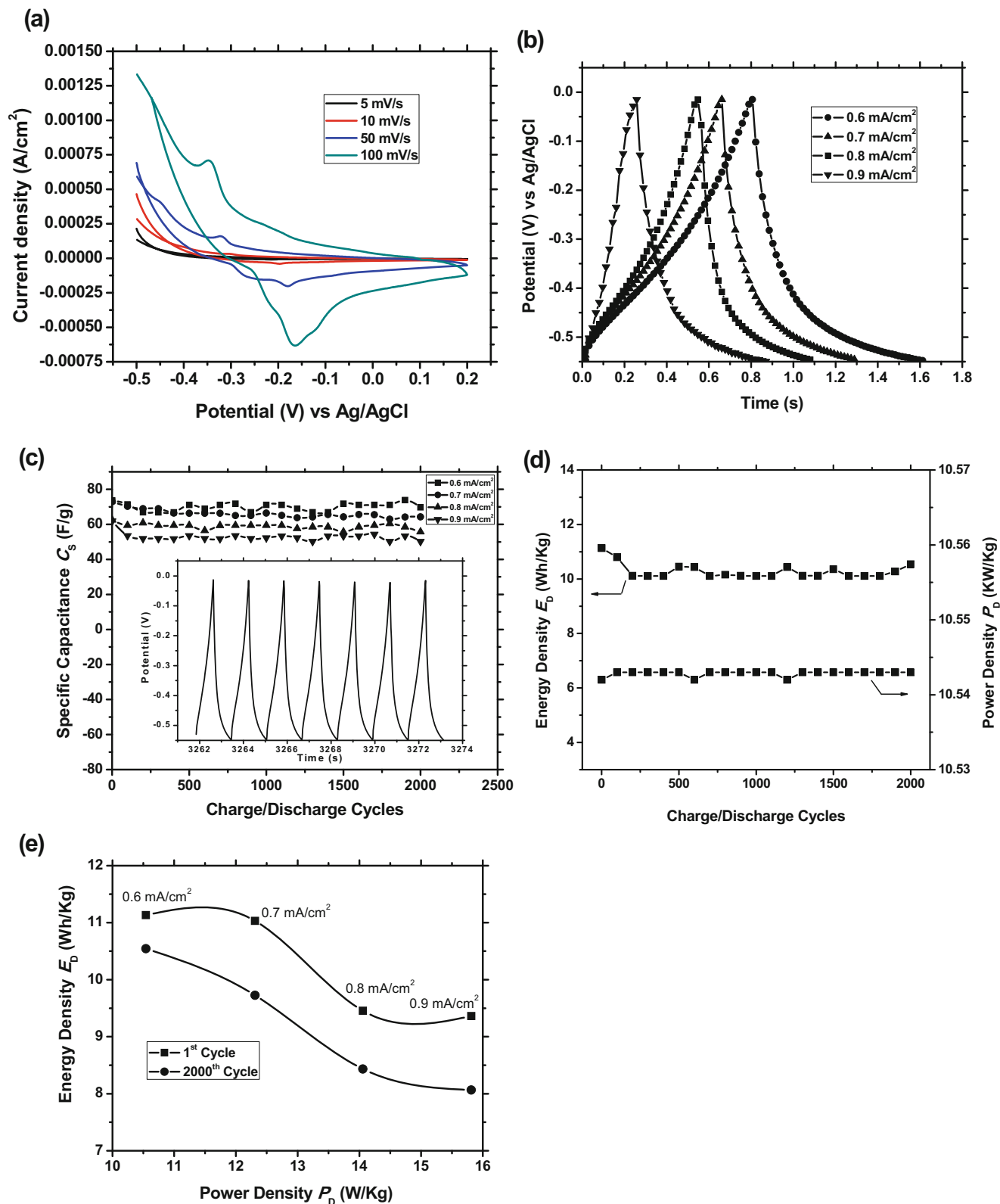


**Fig. 10** **a** Cyclic Voltammograms at different scan rates of  $\alpha$ -MoO<sub>3</sub> thin film prepared at 673 K substrate temperature. **b** Galvanostatic charge/discharge curves recorded at different current densities for the electrode prepared at 673 K substrate temperature. **c** Plot of specific capacitance of the  $\alpha$ -MoO<sub>3</sub> thin film electrode for different applied current densities vs. cycle number and inset figure is last few cycles of fast charge/discharge at

0.6 mA/cm<sup>2</sup> current density. **d** Plot of energy density and power density vs. cycle number at current density 0.6 mA/cm<sup>2</sup> of  $\alpha$ -MoO<sub>3</sub> thin film electrodes prepared at 673 K temperature at different current density. **e** Ragone plot for the 1<sup>st</sup> and 2000<sup>th</sup> cycles of GCD at different current densities of  $\alpha$ -MoO<sub>3</sub> electrode prepared at 673 K substrate temperature



within potential window 0.55 V for  $\alpha$ -MoO<sub>3</sub> thin film electrodes prepared at 673 K substrate temperature. Figure 10c depicts that  $\alpha$ -MoO<sub>3</sub> electrodes show a nonlinear charge/discharge curve, indicating that they have a mainly pseudocapacitive behavior and same graphical nature was reported by few authors [48, 49]. The values of total specific capacitance ( $C_s$ ) are calculated from Eq. (13) [50–53]:

$$C_s = \frac{I \times t_d}{m \times \Delta V} \quad (14)$$

where  $I$  (mA) is the discharge current density,  $\Delta V$  (V) is the working potential window,  $m$  (g) is the actual mass deposited on the active area of the material, and  $t_d$  (s) is the discharging time. The specific capacitance values are calculated to be 73.61, 72.93, 62.51, and 61.9 F/g corresponding to the discharging current densities 0.6, 0.7, 0.8, and 0.9 mA/cm<sup>2</sup>, respectively. It is due to the inner active sites of the electrode which can be fully accessed and diffused with alkali cations at the low current density and also attributed to the slow rate of redox reactions [54]. The variation in the specific capacitance with the cycle number for different current densities is shown in Fig. 10c. The maximum specific capacitance observed for  $\alpha$ -MoO<sub>3</sub> thin film electrode for the 1st cycle is 73.61 F/g and for the 2000th cycle is 69.70 F/g at a 0.6 mA/cm<sup>2</sup> current density. Hence, there is about 95% stability of the  $\alpha$ -MoO<sub>3</sub> thin film electrode deposited at substrate temperature 673 K.

The specific energy density ( $E_D$ ) and specific power density ( $P_D$ ) of the supercapacitor cell were calculated according to the following equation [52]:

$$E_D = \frac{Q \times \Delta V}{2m} \quad (15)$$

$$P_D = \frac{E}{t_d} \quad (16)$$

where  $Q = (I \times t)$  is charge delivered during discharge,  $\Delta V$  is the cell voltage (potential window) and  $t_d$  is the discharging time. The variation of power density and energy density with cycle number is shown in Fig. 10d. Figure 10 depicts very slight variation in energy density and power density after 2000th cycles, it resulted that deposited material have good stability. Figure 10e shows the Ragone plot of  $\alpha$ -MoO<sub>3</sub> electrode deposited at substrate temperature 673 K and shows the highest energy density 11.13 Wh/kg with power density 10.54 kW/kg at applied current density of 0.6 mA/cm<sup>2</sup>.

## Conclusions

Nanostructured  $\alpha$ -MoO<sub>3</sub> electrodes were deposited with different substrate temperatures on the conducting glass substrates by spray pyrolysis technique. The effect of substrate temperature on the microstructural, morphological, optical, electrical, and

electrochemical properties of  $\alpha$ -MoO<sub>3</sub> thin films was investigated. The XRD results revealed that microstructural properties changed with substrate temperature. The optical band gap energy varied in the range 2.56–2.85 eV is observed and it depends on the substrate temperature. The decreasing trend of electrical resistance attributed to the semiconducting nature of the  $\alpha$ -MoO<sub>3</sub> electrode. The spray deposited  $\alpha$ -MoO<sub>3</sub> thin film electrodes at 673 K have successfully showed as supercapacitor property with higher specific capacitance of 73.61 F/g, energy density (11.13 Wh/kg) at the power density 10.54 kW/kg. It is concluded that the electrochemical properties of  $\alpha$ -MoO<sub>3</sub> electrode are temperature-dependent and it can be used for application in electrochemical supercapacitors.

**Acknowledgements** Dr. R. J. Deokate is thankful to the Science and Engineering Research Board, Department of Science and Technology (SB/FTP/PS-079/2014), New Delhi, India, for the financial support through the project under the SERC Fast Track Scheme for Young Scientist (File No. SB/FTP/PS-079/2014).

## References

1. Sayede A, Amriou T, Pemisek M, Khelifa B, Mathieu C (2005) An ab initio LAPW study of the  $\alpha$  and  $\beta$  phases of bulk molybdenum trioxide, MoO<sub>3</sub>. *Chem Phys* 316:72–82
2. Rahmani MB, Keshmiri SH, Yu J, Sadek AZ, Al-Mashat L, Moafi A, Latham K, Li YX, Wlodarski W, Kalantar-zadeh K (2010) Gas sensing properties of thermally evaporated lamellar MoO<sub>3</sub>. *Sensors Actuators B* 145:13–19
3. Wang H, Lin J, Shen ZX (2006) Polyaniline (PANi) based electrode materials for energy storage and conversion. *Journal of Science: Advanced Materials and Devices* 1:225–255
4. Simon P, Gogotsi Y (2008) Materials for electrochemical capacitors. *Nat Mater* 7:845–854
5. Yang P, Sun P, Mai W, (2016) Electrochromic energy storage devices 19:394–402
6. Subramanian V, ZhuH VR, Ajayan PM, Wei B (2005) Hydrothermal synthesis and pseudocapacitance properties of MnO<sub>2</sub> nanostructures. *J Phys Chem B* 109:20207–20214
7. Perera SD, Patel BN, Nijem K, Roodenko O, Seitz JP, Ferreris YJ (2011) Vanadium oxide nanowire–carbon nanotube binder-free flexible electrodes for supercapacitors. *Adv Energy Mater* 1:936–945
8. Hu CC, Chang KH, Lin MC, Wu YT (2006) Design and tailoring of the nanotubular arrayed architecture of hydrous RuO<sub>2</sub> for next generation supercapacitors. *Nano Lett* 6:2690–2695
9. Chen P, Chen H, Qiu J, Zhou C (2010) Inkjet printing of single-walled carbon nanotube/RuO<sub>2</sub> nanowire supercapacitors on cloth fabrics and flexible substrates. *Nano Res* 3:594–603
10. Meher SK, Rao GR (2011) Ultralayered Co<sub>3</sub>O<sub>4</sub> for high-performance supercapacitor applications. *J Phys Chem C* 115: 15646–15654
11. Kim S, Lee J, Ahn H, Song H, Jang J (2013) Facile route to an efficient NiO supercapacitor with a three-dimensional nanonetwork morphology. *ACS Appl Mater Interfaces* 5:1596–1603
12. Tao T, Glushenkov AM, Zhang C, Zhang H, Zhou D, Guo Z, Liu HK, Chen Q, Hub H, Chen Y (2011) MoO<sub>3</sub> nanoparticles dispersed uniformly in carbon matrix: a high capacity composite anode for Li-ion batteries. *J Mater Chem* 21:9350–9355
13. Shen Y, Xiao Y, Yan P, Yang Y, Hu F, Li Z (2014) Hydrothermal deposition and the photochromic properties of molybdenum oxide

- hydrate (MoO<sub>3</sub>(H<sub>2</sub>O)<sub>0.69</sub>) films induced by D, L-malic acid. *J Alloys Compd* 588:676–680
14. Cho YH, Ko YN, Kang YC, Kim ID, Lee JH (2014) Ultrasensitive and ultrasensitive detection of trimethylamine using MoO<sub>3</sub> nanoplates prepared by ultrasonic spray pyrolysis. *Sensors Actuators B* 195:189–196
  15. Osterwald C, Cheek G, DuBow JB (1979) Molybdenum trioxide (MoO<sub>3</sub>)/silicon photodiodes. *Appl Phys Lett* 35:775–776
  16. Wang Y, Zhu Y, Xing Z, Qian Y (2013) Hydrothermal synthesis of  $\alpha$ -MoO<sub>3</sub> and the influence of later heat treatment on its electrochemical properties. *Int J Electrochem Sci* 8:9851–9857
  17. Ferroni M, Guidi V, Martinelli G, Sacerdoti M, Nelli P, Sberveglieri G (1998) MoO<sub>3</sub>-based sputtered thin films for fast NO<sub>2</sub> detection. *Sensors Actuators B* 48:285–288
  18. Diskus M, Nilsen O, Fjellvag H (2011) Growth of thin films of molybdenum oxide by atomic layer deposition. *J Mater Chem* 21:705–710
  19. Dhanasankar M, Purushothaman KK, Muralidharan G (2010) Optical, structural and electrochromic studies of molybdenum oxide thin films with nanorod structure. *Solid State Sci* 12:246–251
  20. Ivanova T, Surtchev M, Geshevam K (2002) Investigation of CVD molybdenum oxide films. *Mater Lett* 53:250–257
  21. Guerrero R, Vargas-Garcia JR, Santes V, Gomez E (2007) Preparation of molybdenum oxide thin films by MOCVD. *J Alloys Compd* 434–435:701–703
  22. Altaman E, Droubay T, Chambers S (2002) Growth of MoO<sub>3</sub> films by oxygen plasma assisted molecular beam epitaxy. *Thin Solid Films* 414:205–211
  23. Boudaoud L, Benramdane N, Desfeux R, Khelifa B, Mathieu C (2006) Structural and optical properties of MoO<sub>3</sub> and V<sub>2</sub>O<sub>5</sub> thin films prepared by spray pyrolysis. *Catal Today* 113:230–234
  24. Sethupathi N, Thirunavukkarasu P, Vidhya VS, Thangamuthu R, Kiruthika GVM, Perumal K, Bajaj HC, Jayachandran M (2012) Deposition and optoelectronic properties of ITO (In<sub>2</sub>O<sub>3</sub>:Sn) thin films by jet nebulizer spray (JNS) pyrolysis technique. *J Mater Sci-Mater Electron* 23:1087–1093
  25. Bouzidi A, Benramdane N, Tabet-Derraz H, Mathieu C, Khelifa B, Desfeux R (2003) Effect of substrate temperature on the structural and optical properties of MoO<sub>3</sub> thin films prepared by spray pyrolysis technique. *Mater Sci Eng B* 97:5–8
  26. Jeyprakash B, Kesavan K, Ashok Kumar R, Mohan S, Amalarani A (2011) Temperature dependent grain-size and microstrain of CdO thin films prepared by spray pyrolysis method. *Bull Mater Sci* 34:601–605
  27. Deokate R, Bhosale C, Rajpure K (2009) Synthesis and characterization of CdIn<sub>2</sub>O<sub>4</sub> thin films by spray pyrolysis technique. *J Alloys Compd* 473:L20–L24
  28. Deokate R, Adsool A, Shinde N, Pawar S, Lokhande C (2014) Structural and optical properties of spray-deposited Cu<sub>2</sub>ZnSnS<sub>4</sub> thin films. *Energy Procedia* 54:627–633
  29. JCPDS data card: 01–0706
  30. Mai L, Hu B, Chen W, Qi Y, Lao C, Yang R, Dai Y, Wang ZL (2007) Lithiated MoO<sub>3</sub> nanobelts with greatly improved performance for lithium batteries. *Adv Mater* 19:3712–3716
  31. Scherrer P (1918) *Göttinger Nachrichten* 2:98–100
  32. Buckley H (1951) *Crystal growth*. John Wiley & Sons, New York
  33. Turgut G, Keskenler EF, Aydın S, Doğan S, Duman S, Özçelik Ş, Gürbulak B, Esen B (2014) Fabrication and characterization of Al/Cu<sub>2</sub>ZnSnS<sub>4</sub>/n-Si/Al heterojunction photodiodes. *Phys Status Solidi A* 211:580–586
  34. Suresh R, Ponnuswamy V, Mariappan R, Senthilkumar N (2014) Influence of substrate temperature on the properties of CeO<sub>2</sub> thin films by simple nebulizer spray pyrolysis technique. *Ceram Int* 40:437–445
  35. He J, Sun L, Zhang K, Wang W, Jiang J, Chen Y, Yang P, Chu J (2013) Effect of post-sulfurization on the composition, structure and optical properties of Cu<sub>2</sub>ZnSnS<sub>4</sub> thin films deposited by sputtering from a single quaternary target. *Appl Surf Sci* 264:133–138
  36. Moses Ezhil Raj A, Lalithambika K, Vidhya V, Rajagopal G, Thayumanavan A, Jayachandran M, Sanjeeviraja C (2008) Growth mechanism and optoelectronic properties of nanocrystalline In<sub>2</sub>O<sub>3</sub> films prepared by chemical spray pyrolysis of metal-organic precursor. *Physica B* 403:544–554
  37. Agashe C, Takwale M, Marathe B, Bhide V (1988) Structural properties of SnO<sub>2</sub>: F films deposited by spray pyrolysis. *Solar Energy Mater* 17:99–117
  38. Barett C, Massalski T (1980) *Structure of metals*. Pergamon Press, Oxford, p 1923
  39. Kireev P (1975) *La Physique des semiconducteurs*. Mir, Moscou
  40. Boudaoud L, Benramdane N, Bouzidi A, Nekerala A, Desfeux R (2016) (MoO<sub>3</sub>)<sub>1-x</sub>(V<sub>2</sub>O<sub>5</sub>)<sub>x</sub> thin films: elaboration and characterization. *Optik* 127:852–854
  41. Welber B, Cardona M, Kim C, Rodriguez S (1975) Dependence of the direct energy gap of GaAs on hydrostatic pressure. *Physics Review B* 12:5729–5738
  42. Ghahramani E, Sipe J (1989) Pressure dependence of the band gaps of semiconductors. *Physics Review B* 40:12516–12519
  43. Tarascon JM, Armand M (2001) Issues and challenges facing rechargeable lithium batteries. *Nature* 414:359–367
  44. Brezesinski T, Wang J, Tolbert SH, Dunn B (2010) Ordered mesoporous  $\alpha$ -MoO<sub>3</sub> with iso-oriented nanocrystalline walls for thin-film pseudocapacitors. *Nat Mater* 9:146–151
  45. Taberna PL, Mitra S, Poizot P, Simon P, Tarascon JM (2006) High rate capabilities Fe<sub>3</sub>O<sub>4</sub>-based Cu nano-architected electrodes for lithium-ion battery applications. *Nat Mater* 5:567–573
  46. Patil SJ, Kumbhar VS, Patil BH, Bulakhe RN, Lokhande CD (2014) Chemical synthesis of  $\alpha$ -La<sub>2</sub>S<sub>3</sub> thin film as an advanced electrode material for supercapacitor application. *J Alloys Compd* 611:191–196
  47. Xiao K, Xia L, Liu G, Wang S, Ding L, Wang H (2013) Honeycomb-like NiMoO<sub>4</sub> ultrathin nanosheet arrays for high-performance electrochemical energy storage. *J Mater Chem A*. doi:10.1039/C5TA00258C
  48. Li D, Liu Y, Lin B, Lai C, Sun Y, Yang H, Zhang X (2015) Synthesis of ternary graphene/molybdenum oxide/poly(p-phenylenediamine) nanocomposites for symmetric supercapacitors. *RSC Adv* 5:98278–98287
  49. Sarfraz M, Aboud MFA, Shakir I (2015) Molybdenum oxide nanowires based supercapacitors with enhanced capacitance and energy density in ethylammonium nitrate electrolyte. *J Alloys Compd* 650:123–126
  50. Conway BE (1999) *Electrochemical supercapacitors: scientific fundamentals and technological applications*. Kluwer Academic/Plenum Publishers, New York, NY
  51. Salunkhe RR, Lin J, Malgras V, Dou SX, Kim J, Yamauchi Y (2015) Large-scale synthesis of coaxial carbon nanotube/Ni(OH)<sub>2</sub> composites for asymmetric supercapacitor application. *Nano Energy* 11:211–218
  52. Han P, Ma W, Pang S, Kong Q, Yao J, Bi C, Cui G (2013) Graphene decorated with molybdenum dioxide nanoparticles for use in high energy lithium ion capacitors with an organic electrolyte. *J Mater Chem A* 1:5949–5954
  53. Deokate RJ, Kalubarme RS, Park CJ, Lokhande CD (2017) Simple synthesis of NiCo<sub>2</sub>O<sub>4</sub> thin films using spray pyrolysis for electrochemical supercapacitor application: a novel approach. *Electrochim Acta* 224:378–385
  54. Zheng L, Xu Y, Jin D, Xie Y (2010) Well-aligned molybdenum oxide nanorods on metal substrates: solution-based synthesis and their electrochemical capacitor application. *J Mater Chem* 20:7135–7143